ADVANCED PHOTONICS RESEARCH Open Access
www.adpr-journal.com

Multipolar Resonances in Electro-Optic Metasurfaces with Moderate Refractive Index

Viktoriia E. Babicheva and Mariacristina Rumi*

The electro-optic (EO) effect is one of the physical mechanisms enabling the dynamic response of metasurfaces, which motivates the analysis of nanoantenna arrays integrated with EO materials. It was shown earlier that chalcophosphate $Sn_2P_2S_6$ metasurfaces can enable significant shifts of multipolar resonances by enhancing the EO response near the Curie temperature. The present work explores how the refractive index of EO materials impacts resonance shifts in metasurfaces with multipolar resonances. It is numerically demonstrated that EO nanoantennas can support pronounced multipolar resonances despite their moderate refractive index, enabling strong light confinement and substantial EO tuning, and that multipolar components of even parity exhibit the highest sensitivity to variations in the refractive index of the nanoantennas. For moderate refractive indices varying from 2.3 to 3.0, it is found that, for a given resonance, the wavelength shift resulting from a refractive index change has a relatively weak dependence on the index itself. This suggests that the refractive index plays only a marginal role in enhancing the EO shift in active photonic devices, and instead, other considerations for material selection, such as the EO coefficient magnitude, the transparency window, and ease of processing, should be of primary concern.

1. Introduction

Metasurfaces, which consist of arrangements of subwavelength optical nanoantennas, have emerged as a versatile platform for manipulating light in ways that are difficult to achieve with traditional optics.[1–9] By engineering the shape, dimensions, and arrangement of these antennas within nanostructures, metasurfaces can control the properties of scattered light, including its phase, amplitude, and polarization.[10] This unique capability has led to a wide range of applications, from flat lenses and holographic displays to beam steering and photonic communication systems. However, one of the key limitations of conventional metasurfaces is that their optical properties are typically fixed once they are fabricated, which restricts their adaptability and dynamic tuning.

Nanoantennas in metasurfaces can support multipolar Mie resonances, which are sensitive to changes in the refractive index of the constituent material. Thus, a mechanism capable of altering the refractive index of nanoantennas in a controllable way can provide the means to tune or reconfigure the metasurface on demand in real time. Recent advances have yielded proof-of-principle demonstrations of the tuning implemented in nanoantennas, providing a promising avenue for developing tunable photonic devices and metasurfaces.[11–13] The specific approaches proposed for tunable metasurfaces are the reorientation of liquid crystals,[14,15] the electro-optic (EO) effect,[16,17] free-carrier modulation,[18] phase changes,[19,20] thermo-optic effects,[21] and others. Electro-optic materials change their refractive index in response to an applied electric-field bias, offering a relatively fast and efficient mechanism to modulate the optical response of metasurfaces in real time. By integrating EO materials within metasurface designs, it is possible to achieve active control over metasurface resonances, switching between different operating wavelengths, and tuning the direction of light scattering.[22–26] The incorporation of EO materials can lead to next-generation photonic devices with enhanced versatility and performance, pushing the boundaries of optical technologies.

We have shown that metasurfaces that include the chalcophosphate $Sn_2P_2S_6$ can exhibit strong multipolar resonances and large resonance tuning with modest electric-field bias due to the enhancement of the EO coefficient near the Curie temperature.[27,28] These promising simulation results, combined with the body of experimental evidence in the literature on the properties of the bulk chalcophosphate $Sn_2P_2S_6$, led us to explore how the physical parameters of the nanoantenna material affect the nature of resonances supported by the metasurfaces and field-induced shifts in resonance positions. Understanding these properties can provide guidelines for material selection at the design stage. In order to take the next step, here, we explore how the unbiased refractive index of the nanoantennas influences the resonance shifts of the nanostructures upon bias.

V. E. Babicheva
Department of Electrical and Computer Engineering
University of New Mexico
Albuquerque, NM 87131, USA
E-mail: vbb@unm.edu

M. Rumi
Air Force Research Laboratory
Materials and Manufacturing Directorate
Wright-Patterson AFB, OH 45433, USA

The ORCID identification number(s) for the author(s) of this article can be found under https://doi.org/10.1002/adpr.202500146.

DOI: 10.1002/adpr.202500146

Table 1. Curie temperatures T_C, refractive indices, and select EO coefficients r, for a series of EO materials. Lithium tantalate $LiTaO_3$, lithium niobate $LiNbO_3$, potassium niobate $KNbO_3$, barium titanate $BaTiO_3$, and bismuth ferrite $BiFeO_3$ are selected because of their significant EO coefficients and interest attracted in the literature, and we include chalcophosphate $Sn_2P_2S_6$ for comparison. This work uses primarily the two materials $BaTiO_3$ and $Sn_2P_2S_6$, which are highlighted in bold. The EO coefficient for $Sn_2P_2S_6$ is taken at a temperature of 2 °C below the Curie temperature; for $BaTiO_3$, r_{131} is at room temperature and r_{333} at 100 °C.

EO material	T_C [°C] [ref.]	Refractive index at 1550 nm [ref.]	r [pm V^{-1}] [ref.]
$KNbO_3$	435[72]	n_a = 2.20, n_b = 2.23, n_c = 2.10[73]	r_{232} □ 450, r_{333} □ 63[74]
$LiTaO_3$	610[75]	n_o = 2.119, n_e = 2.123[76]	r_{333} □ 31[77]
$LiNbO_3$	1195[75]	n_o = 2.21, n_e = 2.14[78]	r_{333} □ 32[63]
$BaTiO_3$	135[79]	n_o = 2.31, n_e = 2.27[80]	r_{131} □ 1000, r_{333} □ 250[65]
$BiFeO_3$	850[81]	n_o = 2.78, n_e = 2.64[82]	r_{333} □ 4.4[83]
$Sn_2P_2S_6$	65[67]	n_1 = 2.78, n_2 = 2.69, n_3 = 2.82[67]	r_{111} □ 1300[67]

A list of selected EO materials is shown in Table 1, where the materials are listed in order of increasing refractive index n at the telecommunication wavelength of 1550 nm, based on the smallest n. It should be noted that the order is approximate because of the different values of the refractive index component in different crystal orientations. The dispersion of the refractive index components of these materials is shown in Figure S1, Supporting Information. Lithium niobate $LiNbO_3$ is the most common EO material due to its well-known properties and well-established fabrication of high-quality thin films and single crystals. Various $LiNbO_3$ metasurface designs have been extensively explored,[29–37] including cases with modulation of the phase and amplitude of scattered light by an external electric-field bias.[16,17,23,38–41] Other EO materials of potential interest are $BaTiO_3$, $KNbO_3$, $LiTaO_3$, $BiFeO_3$, and $Sn_2P_2S_6$, all of which have a moderate refractive index (see Table 1). Among these materials, $Sn_2P_2S_6$ and $BiFeO_3$ have the highest refractive indices.

Although nanoantennas made of materials with moderate refractive index have been shown to support Mie resonances,[42] a higher refractive index is desirable for metasurfaces. It allows for better light confinement and stronger resonances due to the higher reflection at the nanoantenna boundaries, leading to a higher fraction of light bouncing at each instance.[43,44] For a plane wave impinging normally on an infinite plane interface of two materials with refractive indices n_1 and n_2, the reflectance coefficient with respect to amplitude is Γ ¼ ðn_1 − n_2Þ=ðn_1 þ n_2Þ, and the intensity quantity is jΓj^2. Thus, for the interface of a high-refractive-index material, such as silicon with n_1 = n_{Si} □ 3.5 and glass with n_2 = n_{SiO2} □ 1.5, the reflectance is $\Gamma_{Si=SiO2}$ □ $\Gamma_{3:5=SiO2}$ □ 0.4 (intensity 0.16). However, for a moderate refractive index material, this value is significantly lower, and the specific examples are $\Gamma_{2:7=SiO2}$ □ 0.29 (intensity 0.08) and $\Gamma_{2:3=SiO2}$ □ 0.21 (intensity 0.04), with the latter being four times less than the case of silicon nanoantenna. More complex processes need to be accounted for to describe light reflection inside nanoantennas, but the plane-interface expression explains why a higher refractive index is important for the formation of nanoantenna resonances and not a mere requirement to reduce the effective wavelength and reach subwavelength characteristic dimensions. Thus, it could be expected that selecting a higher refractive index would enhance optical field interactions, facilitate a stronger shift of nanoantenna resonances, and improve device performance. However, a quantitative analysis of such shifts for different initial refractive indices of the nanoantennas has not yet been reported, and this motivates the EO metasurface analysis carried out in this work.

This work focuses on embedding EO functionality within metasurfaces to impart tunability of their optical response and computationally investigate the properties of multipolar nanoantenna arrays (Figure 1) depending on the refractive index and the lattice period. EO metastructures can be realized either by patterning directly the EO material[16,24,45,46] or by using a uniform layer of EO material underneath a nonactive nanostructured layer, often made of more conventional materials.[17,23,47,48] Shifts in resonance positions are achievable in both cases. In general, patterning of a polymer or silicon layer deposited on top of an EO material should be more straightforward to achieve, as recipes are known, than patterning a novel or rarely used material. In the case of patterned EO materials, the application of a voltage would change the refractive index of the active areas of the nanostructure, resulting in a change of refractive-index contrast for interfaces in all directions (above, below, and within the layer). In the case of a uniform EO layer, only the refractive index contrast at one interface would be changed by the EO effect (the empty spaces between nanoantennas would remain unchanged).

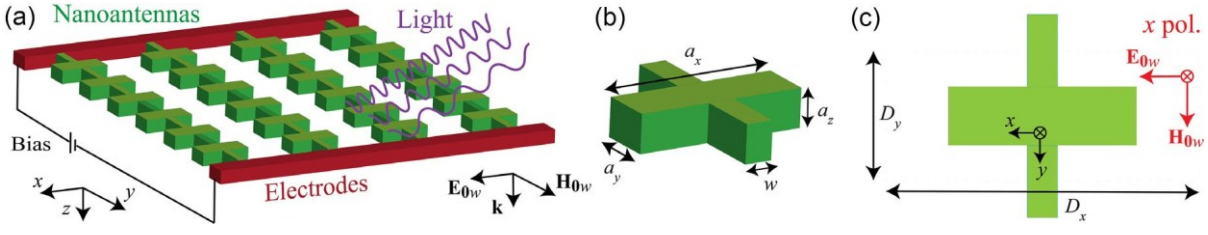

Figure 1. Metasurface consisting of bridged nanocuboids made of an EO crystal with a refractive index n. The nanocuboids are arranged on a silica substrate with the refractive index n_{sub} = n_s and covered by an index-matching superstrate with n_{super} = n_{sub} = n_s (not shown because the refractive index matches that of the substrate, ensuring uniformity). a) Nanoantenna array with electrodes connected to the nanocuboids and their bridges at both ends along the y-axis. b) Single nanocuboid with the dimensions a_i (i = x,y,z) and a bridge of fixed width w = 80 nm. c) Top view of the unit cell (with lattice periods D_x and D_y), depicting the orientation of the incident light fields relative to the nanocuboid and the bridge.

This could affect the interference of waves within the plane of the structure, and thus the nature or position of the resonances. For this work, we choose the case of patterned EO materials.

We consider mainly the range of moderate refractive indices that includes known EO materials in Table 1 (n = 2.2–2.7). Some simulations are also performed for higher indices to determine if trends extend to these values, even if the options for EO materials are very limited or nonexistent. In general, integrating materials characterized by a significant EO coefficient in metasurfaces is desirable because a larger modulation of their refractive index can be achieved for a given external electric field. Here, we aim to separate the effect of the unbiased value of the refractive index from the magnitude of the bias-induced refractive index change and determine whether they might lead to separate advantages in material selection. Our simulations indicate that resonances are excited at longer wavelengths in metasurfaces with a higher refractive index, and these resonances are more pronounced, with the strongest resonances observed for the highest refractive index. Using the framework of multipolar analysis, we show that multipolar components categorized as even, such as the magnetic dipole (MD) and electric quadrupole (EQ), are most responsive to changes in the refractive index of the nanoantennas. We also numerically demonstrate the effect of changes in permeability introduced artificially, and we observe that the electric dipole (ED) and magnetic quadrupole (MQ), both categorized as multipoles of odd parity, are most responsive to these changes. This agrees well with our computations of electric and magnetic energy values, where the resonances of multipoles with odd parity mainly enhance the latter. The results of this work provide insight into how to optimize material selection and functional design for next-generation tunable metasurfaces, facilitating more adaptable and versatile optical technologies.

2. Numerical Analysis and Multipolar Decomposition

Our analysis is centered on understanding the relation between the refractive index of nanoantenna's EO materials and the behavior of multipolar Mie resonances in these nanoantenna arrays under EO modulation, which offers metasurface tunability for optoelectronic applications. We explore approaches to achieve effective, real-time control over the resonances of these metasurfaces by selecting EO materials and optimizing the design parameters, identifying trends that could inform the design of tunable photonic devices. Specifically, we vary the refractive index of the constituent material n, compute the resonances of the nanostructures, and quantify the resulting resonance shifts $\Delta\lambda$. Unless stated otherwise, the refractive index change Δn in the EO material is introduced through the change in the material's permittivity, which is always the case for materials in the optical spectral range. Section 4.3 discusses the effect of introducing Δn through the change in the material's permeability to understand changes in the multipoles of electric and magnetic nature. In numerical simulations, nanoscatterers are nanocuboids with dimensions a_x, a_y, and a_z. The wavelength range of interest is from 1000 to 2500 nm. A nanoscatterer in the elementary cell is modeled with repeating boundaries along the x- and y-directions, simulating an infinite array of identical nanoantennas. The built-in Floquet–Bloch boundary settings are utilized to model periodic configurations by imposing phase consistency at the edges, ensuring that optical waves in the computational domain have repetitive spatial variation. The full-wave electromagnetic simulations are performed using the frequency-domain solver with steady-state response of periodic nanostructures in the CST Studio Suite. The metasurface unit cell, consisting of a single nanoantenna in an index-matched substrate–superstrate environment, is modeled within a simulation domain bounded by periodic boundary conditions in the in-plane directions, thereby representing an infinite periodic array. The illumination is realized by a normally incident plane wave, and the ports are placed along the propagation direction to record the transmitted and reflected fields. This approach captures the interaction of incident light with an effectively infinite periodic structure, including diffractive effects, the Rayleigh anomaly, and the collective multipolar response. Replication of an infinitely homogeneous environment is achieved by implementing sufficiently thick artificial perfectly matched layers along the direction of incident wave propagation. These perfectly matched layers are positioned along the z-axis with a separation of 10 μm, functioning as excitation and detection planes for waves propagating into the far-field zone.

In our work, nanoantenna performance is defined as the effectiveness of the nanoantenna in shifting its resonance spectrally in response to a given change in the refractive index of its constituent material. This measure directly quantifies the metasurface's tunability in response to the EO effect in the nanoantenna material. Alternatively, nanoantenna performance can also be evaluated in terms of how well the nanoantenna localizes and enhances light because these factors influence field confinement and interaction strength, which can indirectly affect resonance tuning. The strength of a nanoantenna resonance is characterized by the degree of field confinement within the nanostructure, leading to an enhanced light-matter interaction.[49,50] This increased localization results in deeper and broader transmittance dips, indicating more efficient coupling of incident waves to resonant modes and stronger suppression of specific spectral components under the resonance conditions.

The nature of nanoantenna resonances is identified by multipolar decomposition, allowing us to distinguish and analyze the contributions of different modes, such as electric and magnetic dipoles, quadrupoles, and higher-order multipoles.[5,51–53] Multipolar decomposition is a crucial analytical tool for understanding and quantifying the optical behavior of nanoantennas, particularly when investigating resonance shifts due to EO effects. We identify which resonances are most sensitive to changes in the refractive index by decomposing the scattered electromagnetic fields into their constituent multipolar components, and we limit the analysis to the first six multipoles (electric and magnetic dipoles ED and MD, quadrupoles EQ and MQ, and electric octupole (EOC) and magnetic octupole (MOC)). This method allows us to isolate the contribution of each mode, providing detailed insights into how the refractive index of the material affects the scattering properties of the nanoantennas. The multipolar decomposition is computed to analyze the behavior of individual nanoantennas and their arrays, as well as the effect of EO tuning. Multipoles can be classified as *even* (with even or positive parity) or *odd* (with odd or negative parity) according to their symmetry under spatial inversion.[54–56] The multipolar moments ED, MQ, and EOC change sign in the inverted coordinate system

and are referred to as multipoles with odd parity. The vector of the ED moment is a "true" vector. In turn, the MD moment vector can be derived through a vector product of two "true" vectors (radius vector and ED moment). Since both "true" vectors change their sign under coordinate inversion, in the new inverted coordinate system, the vector has positive coordinates. Such vectors are referred to as pseudovectors (axial vectors). The multipolar moments MD, EQ, and MOC retain the sign of their components under inversion operation and are thus referred to as multipoles with even parity. Even multipoles, such as MD and EQ, exhibit symmetric electric field distributions, while odd multipoles, including ED and MQ, exhibit asymmetric field distributions, meaning that the electric fields in the r and −r directions have π phase difference. This classification determines the spatial distribution of electromagnetic fields and their coupling efficiency with external excitation.

3. Individual Nanoantennas

To start with, we consider isolated cuboid nanoantennas (Figure 1b) with $a_x = a_y = a_z = 720$ nm made of materials with different refractive indices. Figure 2a shows the absorption cross-sections of such nanoantennas. The horizontal lines in the figure approximately correspond to some common EO crystals: $n = 2.3$ (close to $BaTiO_3$), $n = 2.7$ (close to $Sn_2P_2S_6$ and $BiFeO_3$), and intermediate values occur widely in other natural materials. As a reminder, within EO materials, lithium tantalate $LiTaO_3$ has $n \approx 2.1$, lithium niobate $LiNbO_3$ and potassium niobate $KNbO_3$ have $n \approx 2.2$, and barium titanate $BaTiO_3$ has $n \approx 2.3$, while bismuth ferrite $BiFeO_3$ and chalcophosphate $Sn_2P_2S_6$ have $n \approx 2.7$ (see Table 1). As the refractive indices of $LiTaO_3$, $LiNbO_3$, $KNbO_3$, and $BaTiO_3$ are lower than the refractive index of $Sn_2P_2S_6$, one can expect that the performance of nanoantennas and EO metasurfaces made of these materials will be worse. For this analysis, the refractive-index dispersion has been neglected but, in practice, the materials are slightly dispersive over the wavelength range of interest here. Previous analysis of $Sn_2P_2S_6$ metasurfaces has shown that dispersion only slightly affects the spectral position of the resonances, but the resonance strength and all the conclusions remain valid (see Supplementary Information for Ref. [27]). In the present analysis, it is important to separate the effect of resonance shifts without the influence of material dispersion (as these conclusions are applicable to other metasurfaces made of similar material) from the effect of dispersion, which is individual to each material. The components of the $Sn_2P_2S_6$ refractive index change maximum by ≈0.11 in the entire range of wavelength of interest (1000–2500 nm), whereas for $BaTiO_3$ the value is only ≈0.06, and thus, the effect of dispersion

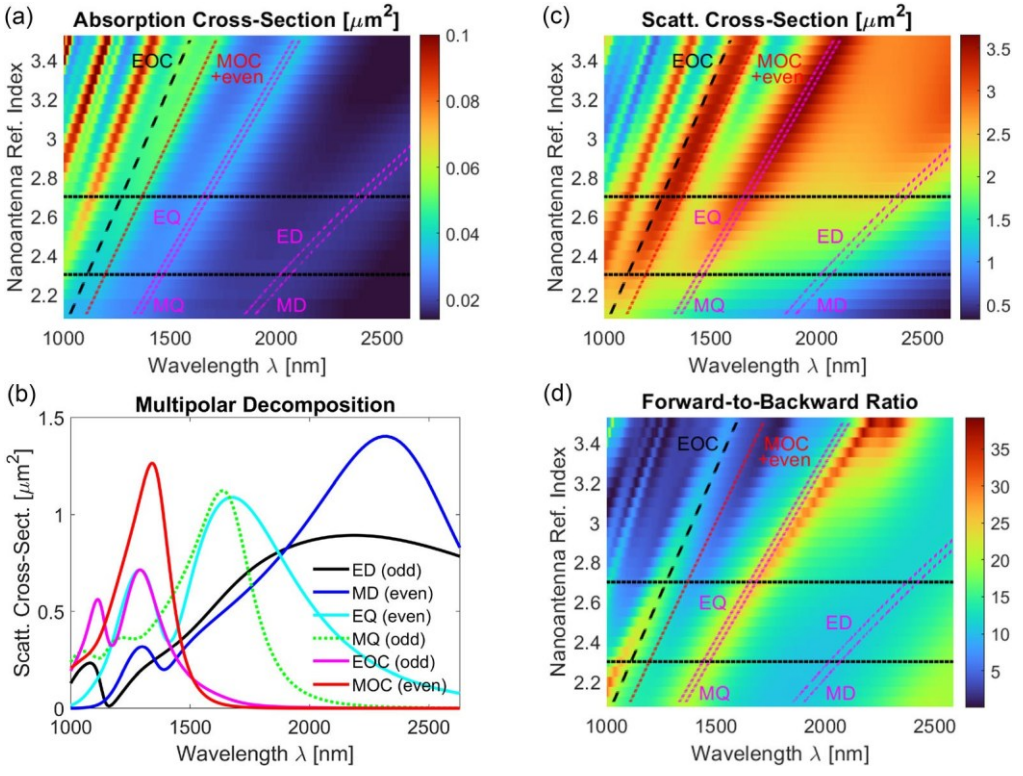

Figure 2. a) Total absorption cross-sections for isolated nanoantennas made of different materials. Nanoantennas are of cuboid shape with dimensions $a_x = a_y = a_z = 720$ nm. Horizontal lines approximately correspond to the common EO crystals discussed in this work ($n = 2.3$ and 2.7). Mode branches are identified as local maxima of the absorption cross-sections (and the lines are guides for the eye). The types of modes are determined from the multipolar decomposition. Here, "E" and "M" stand for electric and magnetic, and "D," "Q," and "OC" stand for dipolar, quadrupolar, and octupolar components, respectively. b) Multipolar decomposition for $n = 2.7$ (≈$Sn_2P_2S_6$) and cuboid with $a_x = a_y = a_z = 720$ nm. Each multipole in the decomposition is characterized by its scattering cross-section, and the ED term includes a toroidal component. c) Total scattering cross-section obtained with full-wave numerical simulations and d) ratio of forward scattering to backward scattering for the same nanoantennas as in panel (a).

with $BaTiO_3$ nanoantennas will be even less than with $Sn_2P_2S_6$ nanoantennas and remain negligible. Electro-optic materials are also anisotropic because of their crystalline structure, and we use an isotropic approximation to understand the most salient features of the nanoantenna multipoles. Similar to the effect of material dispersion, simulations of $Sn_2P_2S_6$ metasurfaces have shown that anisotropy only marginally shifts the resonance wavelength, while the resonance strength and overall conclusions remain unchanged (see Supplementary Information for Ref. [27]). In this work, again, it is essential to distinguish the resonance shift associated with nanoantenna dimensions and EO effects from anisotropy effects, which are material-specific and present even in the absence of electrical bias.

Mode branches are identified as the local maximum values of the absorption cross-sections. From the simulation results in Figure 2a, we observe that the resonances of all multipolar components experience a redshift with an increase in the refractive index of the nanoantenna. The dipolar resonances are broad and spectrally close, almost overlapping. Quadrupolar resonances are narrower than the dipolar ones, but also spectrally close and comparable in magnitude. Octupolar resonances, as well as secondary dipolar and quadrupolar resonances, are excited at a shorter wavelength.

Figure 2b shows the multipolar components obtained for $n = 2.7$ ($\square Sn_2P_2S_6$) and a nanocuboid with $a_x = a_y = a_z = 720$ nm. The dipolar components have the strongest contribution to the scattering cross-section. Analysis of the total scattering cross-section (Figure 2c) and the ratio of forward to backward scattering (Figure 2d) for the same nanoantennas reveals pronounced resonances, which become increasingly prominent as the refractive index of the material increases. Dipolar and quadrupolar resonances are particularly strong, and these resonances are sensitive to material properties, with higher refractive indices leading to stronger light-matter interactions. This enhancement highlights the critical role of the refractive index in shaping the scattering from the nanoantenna, not only in terms of magnitude but also in terms of directionality of the scattered light. The forward-to-backward ratio of the scattered light intensity can reach as high as 35 (Figure 2d), and this enhancement occurs in proximity to the EQ and MQ resonant excitations, where not only the ratio, but also the total scattering, is high due to proximity to the resonances. This behavior shows the potential of EO materials in tailoring the optical characteristics of nanoantennas through effective control of resonant features. For individual nanoantennas, the results demonstrate that a higher refractive index leads to stronger resonances, highlighting the particular advantage of using $Sn_2P_2S_6$, or other high-index materials.

4. EO Metasurfaces

We then perform numerical simulations of the optical properties of metasurfaces consisting of nanoantenna arrays of various periodicities and refractive indices (Figure 1). The nanoantennas are linked by a narrow bridge along the y-direction. The incident light is linearly polarized along the x-direction. If nanoantennas, or building blocks, are made of EO materials, the resulting metasurface can be dynamically switched by applying suitable electric fields to achieve tunable metasurface responses. The primary focus here is on the effect of the antenna's refractive index on the type of resonances excited in the array, the tuning range resulting from the Pockels effect, and the magnitude of mode confinement. To incorporate realistic elements, we design nanoantenna metasurfaces positioned on a substrate with a refractive index of $n_s = 1.47$ (equivalent to silica). The nanoantennas are covered on the top and the sides with the same material.

We compute the properties of metasurfaces made of EO material with $n = 2.7$ ($Sn_2P_2S_6$) and $n = 2.3$ ($BaTiO_3$) (Figure 3). In the transmittance spectral maps, the wavelengths of the Rayleigh anomaly $\lambda_{RA} = n_s D_x$ are shown by diagonal dashed white lines. We observe that all spectral features move with a change in the array period (Figure 3a,b). The sharp features in the metasurface spectra should result in more pronounced changes under the EO effect, and we quantify this effect in the subsequent analysis.

Similarly to the case of isolated nanoantennas, the resonances supported by the metasurfaces are categorized based on a multipolar decomposition (Figure 3c,d). Because of the lattice, even and odd multipoles can couple to each other, resulting in combined resonances, such as EDþMQ (odd) and MDþEQ (even). Analyzing the multipolar decomposition, one can see that the features appear in all odd or even multipoles at the same wavelength, but there is virtually no cross-multipolar coupling (no features in the odd multipole spectra at the spectral position of even multipole resonances and vice versa). The distributions of E_w- and H_w-fields obtained with numerical simulations at the two wavelengths of the EDþMQ (odd) and MDþEQ (even) resonances indicate profiles corresponding to typical electric and MDs, respectively (Figure 4). The electric and magnetic octupolar components are relatively weak. Similar trends are observed in the simulations of the transmittance spectra and the calculations of the multipolar decomposition for the metasurfaces with $n = 3.0$ (Figure S2, Supporting Information).

We also compare the transmittance of the metasurfaces with different bridge directions: "y-axis bridge" as the one shown in Figure 1 (assumed in all other numerical simulations in this work) and "x-axis bridge," allowing connections in the x-direction, but maintaining light polarization along the x-direction in both cases. We observe that when the array period is small, the changes in the spectra are minimal (Figure S3a, Supporting Information). The larger period of the array results in larger changes between the two cases (Figure S3b, Supporting Information), but the spectra are qualitatively similar and exhibit the same set of multipolar resonances. It is reasonable to assume that the conclusions regarding general trends associated with the array parameters and refractive index obtained for metasurfaces with bridges in the y-direction are applicable to metasurfaces with bridges in the x-direction.

Collective resonances in nanoantenna arrays can emerge even in arrays with as few as 7 × 7 elements and converge closely to the response of infinite arrays for sizes of □10 × 10 to 20 × 20 elements.[57,58] Given the □1 μm period of our design, a metasurface with lateral dimensions of 10–20 μm would adequately support the resonance behavior while providing a spacing between the coplanar electrodes that would allow us to reach the necessary effective electric field in the nanoantennas by applying realistic voltages. Similar metasurface configurations incorporating $LiNbO_3$ have been realized experimentally within this size range of 10–20 μm,[16,39] validating the practicality of the proposed electrode spacing and device dimensions.

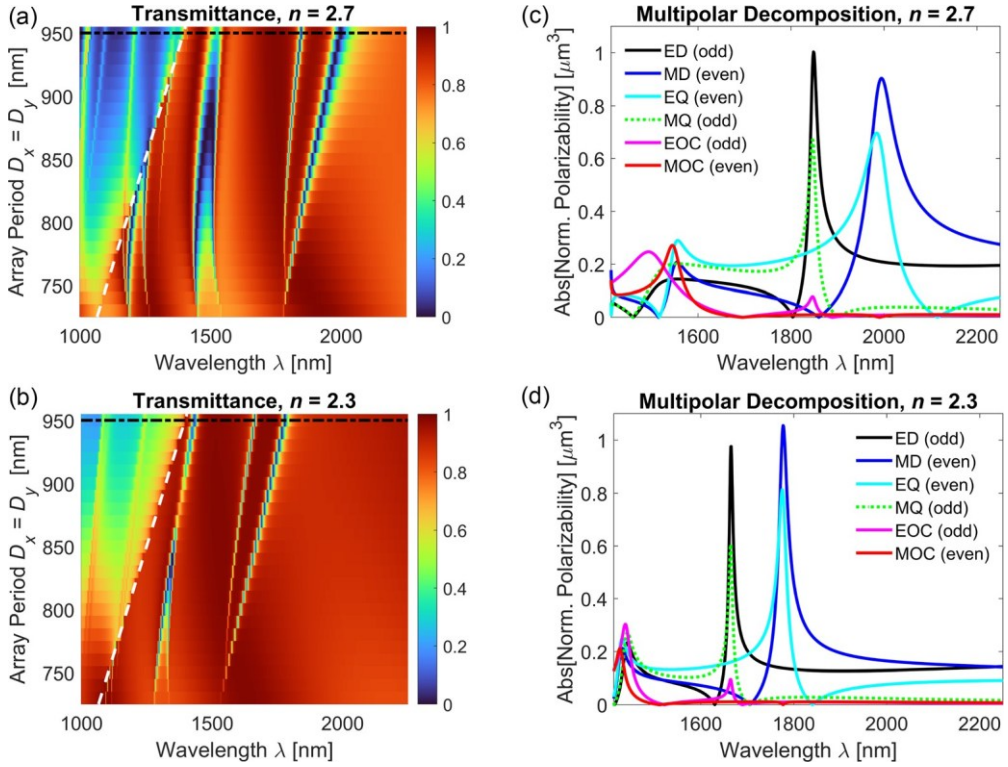

Figure 3. a,b) Transmittance and c,d) multipolar decomposition for metasurfaces made of different EO materials: (a,c) $n = 2.7$ ($Sn_2P_2S_6$) and (b,d) $n = 2.3$ ($BaTiO_3$). The wavelengths of the Rayleigh anomaly $\lambda_{RA} = n_s D_x$ are denoted by the diagonal dashed white lines. Black horizontal dot-dashed lines show $D_x = D_y = 950$ nm corresponding to the multipolar decompositions in panels (c,d). In all panels, nanocuboids have $a_x = a_y = a_z = 720$ nm, and they are connected by bridges of $w = 80$ nm.

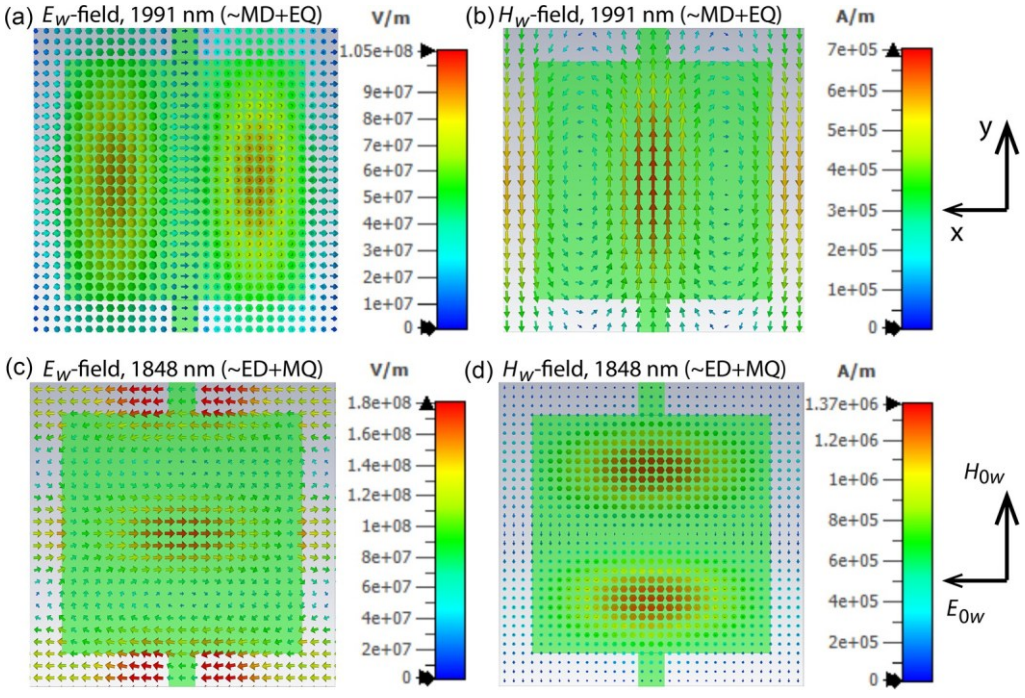

Figure 4. Field distributions for two multipolar resonances from numerical simulations. a) E_w-field and b) H_w-field at wavelength 1991 nm corresponding to MDþEQ, c) E_w-field and d) H_w-field at 1848 nm corresponding to EDþMQ. Metasurface is made of an EO material with $n = 2.7$ ($Sn_2P_2S_6$). Array periods are $D_x = D_y = 950$ nm. Nanocuboids have $a_x = a_y = a_z = 720$ nm, and they are connected by bridges of $w = 80$ nm.

4.1. Multipolar Spectral Features

We observe that zeros occur in the spectral profiles in Figure 3c,d, and these can be explained as follows. Whether we analyze the nanoantenna's effective polarizability, absorption, scattering, or extinction cross-section corresponding to each multipolar component, zeros can occur in the spectral profile even for the simplest nanoantenna, which is an individual spherical particle without dispersion or anisotropy of the constituent material. It is difficult to understand the origin of spectral zeros on an intuitive level because analytical solutions are based on special functions (such as Bessel and Hankel functions), but zeros can occur because of the destructive interference of scattered fields. Each multipolar resonance arises from the interaction between the incident wave and the nanoantenna. At specific nanoantenna dimensions relative to the wavelength, the contributions from different parts of the induced current distribution can interfere destructively, leading to a zero in the particular cross-section or polarizability of that multipolar component. In configurations more complex than individual nanoantennas, a zero spectral response is often observed for nanoantenna arrays with the collective effect of multipoles of the same type without cross-multipolar coupling.[3,59] This spectral feature occurs mainly because of the collective lattice effect and the interplay of the lattice sum of the particular multipole with the spectral response of the individual nanoantenna in the array. The zero usually occurs in proximity to or right at the Rayleigh anomaly, which is an anomaly indicating the emergence of a new diffraction order propagating along the lattice plane.

The Rayleigh anomaly arises when a diffracted order of light from a periodic metasurface transitions between propagating and evanescent regimes, occurring at wavelengths determined by the lattice period and the surrounding refractive indices.[3–5,57,60] In the case of the metasurface being a periodic array of EO crystal nanoantennas with equal periods and index-matched substrate and superstrate, the Rayleigh anomaly manifests as a sharp spectral feature associated with the onset of a grazing diffraction order. Its physical significance lies in the strong redistribution of electromagnetic energy under this condition, which can enhance or suppress specific mode excitations through diffractive coupling. While lower-order multipolar resonances (dipoles and quadrupoles) lie at relatively longer wavelengths and remain largely unaffected, higher-order multipoles positioned near the Rayleigh anomaly experience pronounced spectral shifts and altered lineshapes, effectively tracking the Rayleigh anomaly position as it moves with changes in lattice parameters or the surrounding refractive index. This interplay between the Rayleigh anomaly and higher-order modes introduces a sensitive control mechanism over spectral dispersion and resonance tuning in the metasurface.

Additional spectral points with zeros can occur in cases of more complex structures and multipolar arrays supporting cross-multipolar coupling. The effect can be investigated using the analytical framework for the spherical particle due to the possibility of including or excluding cross-multipolar terms in analytical expressions.[59] Analysis of the spherical particles is particularly instrumental as there are no analytical expressions for disk or cuboid particles, and separation of cross-multipolar terms is not possible. Similar to the previous analysis of spherical particles,[59] the present investigation of nanocuboids shows that if the magnitude of one of the multipolar components is small, it can drop to zero due to the cross-multipolar coupling, as is the case for dipoles and quadrupoles in Figure 3c,d. Without coupling, the resonant response follows a symmetric Lorentzian shape. However, due to coupling, the spectral profiles become asymmetric and reach zero at certain wavelengths. In each pair, for example, the pair of odd multipoles ED and MQ or the pair of even multipoles MD and EQ, two multipolar spectra are distorted in opposite directions. For example, in both panels of Figure 3c,d, the effective polarizability of ED reaches zero on the blue side with respect to the maxima of ED and MQ, while the MQ polarizability reaches zero on the red side of the ED and MQ resonances. The same is observed for the pair of MD and EQ. The interaction is not limited to the pair of dipole and quadrupole, and the contribution of octupoles is included, but only for the shorter wavelength, as they are insignificant at the wavelength where the dipoles and quadrupoles experience the strongest resonances. We also perform multipolar decomposition for an alternative value of the array period ($D_x = D_y = 850$ nm, see Figure S4a–c, Supporting Information), and observe the same trend as in Figure 3c,d for $D_x = D_y = 950$ nm.

4.2. Tunability

Analyzing the transmittance and mode strength, we observe that nanoantennas made of materials with a higher refractive index allow for higher mode localization and more drastic changes in the transmittance spectra, for example, broader dips. The mode localization is determined by introducing a negligible loss coefficient in the nanoantenna material and then simulating the resulting absorptance of the metasurfaces (the results are presented in Figure S4d–f, Supporting Information). After identifying the nature of metasurface resonances, we analyze the shift of each multipolar resonance for EO metasurfaces with different refractive indices as a function of the array period (Figure 5 and S5, Supporting Information). The data is extracted from the simulations and paired with another set of simulations for the altered refractive index of nanoantennas: The initial simulation set is for nanoantennas with refractive index n, and the second set is for n þ Δn, where $\Delta n = 0.05$. Tracing maxima of mode localization provides more accurate information about the position of the resonance compared to tracing dips in the transmittance, as the latter is prone to interference when two resonances are spectrally close. Figure S4d–f, Supporting Information, shows a clear distinction between even and odd resonances, while the transmittance spectra in Figure 3a,b show their combined effects. Thus, we track the spectral position of the absorptance maxima for each resonance and calculate its shift when the nanoantenna material index changes by $\Delta n = 0.05$ (Figure 5a,b).

Let us analyze the effect of different multipoles on the shift of the peak, referring to dipoles and quadrupoles (that is, MDþEQ and EDþMQ) as the lowest-order multipolar components and octupoles as higher-order multipolar components. For the smallest lattice period (that is, the densest array), the lowest-order multipolar resonances experience the most significant shift for all EO materials, and this shift is in the range of $\Delta\lambda$ □ 30–32 nm. For the smallest period of □730–740 nm, one can see only tiny

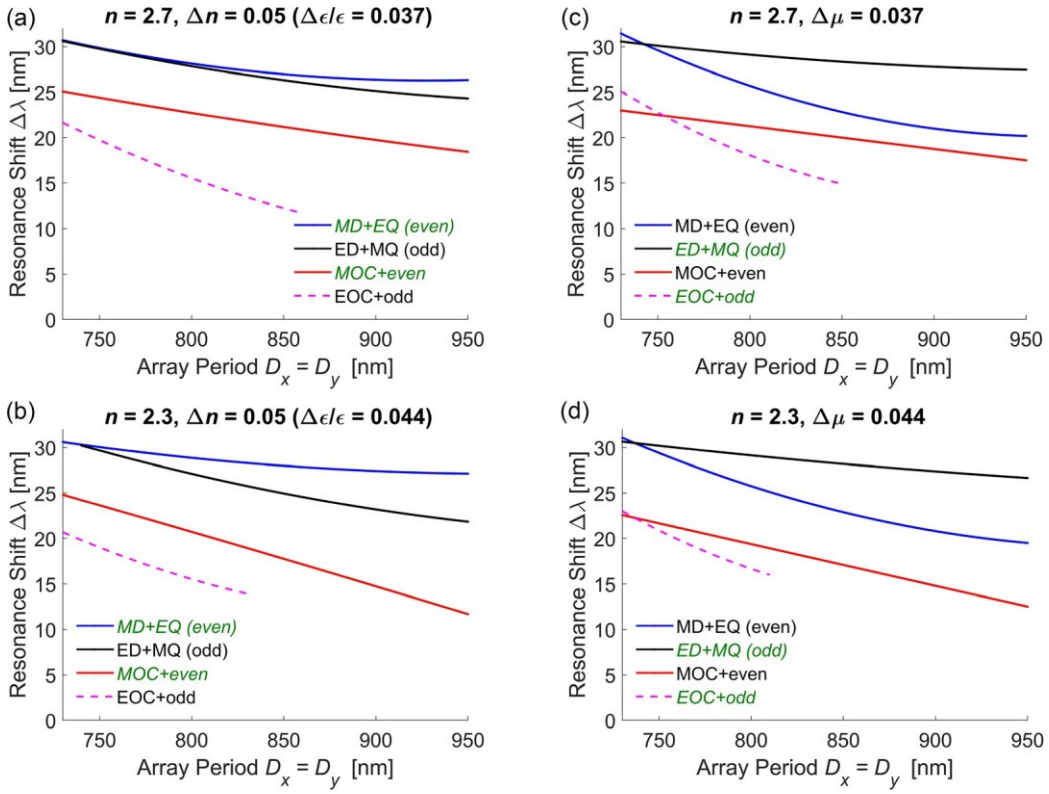

Figure 5. Analysis of how each resonance behaves under changes in refractive index: Wavelength shift of each multipolar resonance $\Delta\lambda$ for metasurfaces made of different EO materials. a,c) n = 2.7 ($Sn_2P_2S_6$) and b,d) n = 2.3 ($BaTiO_3$). (a,b) Resonance shift $\Delta\lambda$ corresponding to a refractive index change Δn = 0.05. (c,d) Resonance shift $\Delta\lambda$ corresponding to a permeability change $\Delta\mu$ whose magnitude (see graph titles) is selected to ensure the preservation of electromagnetic duality for each material. In all panels, nanocuboids have $a_x = a_y = a_z$ = 720 nm, and they are connected by bridges with w = 80 nm.

differences in the resonance shifts for each resonance type in all refractive indices under consideration. If we consider larger periods of 740–950 nm, the higher-order multipoles have smaller shifts than the lowest-order multipoles, and the decrease is most drastic for materials with a lower refractive index. For n = 3.0, the shift of MOC and other even multipoles is still substantial and $\Delta\lambda$ 20–25 nm (Figure S5, Supporting Information). It is worth pointing out that the MDþEQ and EDþMQ shifts are nearly identical in dense arrays, but they begin to separate as the period increases, and the separation becomes more pronounced at lower n. From these results, we observe that for materials with a higher refractive index, such as $Sn_2P_2S_6$, the resonance shift remains strong for all lattice periods, suggesting that such EO metasurfaces should have better tunability or the ability to discriminate input signals over those made of materials with a lower refractive index, such as $BaTiO_3$ or $LiNbO_3$.

When the shifts of resonances that stem from different lowest-order multipoles are compared, one can see that for n = 2.3 and 2.7, those linked to even multipoles MDþEQ are more sensitive to changes in refractive index than those linked to odd multipoles EDþMQ. In contrast, for n = 3.0, the EDþMQ resonance experiences a slightly larger shift than the MDþEQ resonance (Figure S5, Supporting Information). Thus, the EDþMQ resonance experiences the most substantial shift for the EO material with a higher refractive index under its variation. For all three cases n = 2.3, 2.7, and 3.0, the shift for MOC and associated even multipoles is larger than for EOC and associated odd multipoles. The shift of MOCþeven multipolar resonances remains significant even for nanoantennas made of EO materials with a lower refractive index.

4.3. Electric and Magnetic Energy

Regardless of whether the multipolar resonance has an electric or magnetic nature, both fields are enhanced at the resonance, and thus, multipolar resonances of the electric nature do not provide a particular advantage relative to magnetic resonances upon a change in the refractive index (linked to the material permittivity). However, there is an asymmetry in the response of even and odd multipoles to the change in the refractive index observed in Figure 5a,b. Using electromagnetic duality, we perform a theoretical analysis of the resonance shift as the material permeability varies (Figure 5c,d). For each EO material, we set $\Delta\mu = \Delta\varepsilon/\varepsilon$, provided that μ = 1, which is common for all materials in the optical range. This selection ensures the matching conditions of relative perturbation and the preservation of electromagnetic duality. Although this change in permeability is too large to be observed in natural materials in the optical range, the analysis is instrumental in understanding the response of the different multipoles to the electromagnetic properties of the materials. An examination of resonance shifts associated with such permeability change for the various multipoles reveals that resonances corresponding

to odd modes EDþMQ exhibit greater sensitivity to changes in the material permeability of the nanoantenna relative to even modes MDþEQ for most of the array periods (the exception is the case of the very small period, which gives the reverse trend). These resonance shifts remain pronounced even in nanoantennas composed of EO materials with relatively low refractive indices.

We calculate the electric and magnetic energy in the metasurface with $n = 2.7$ (Figure 6). After normalizing the two spectral profiles to ensure equal energy in the even MDþEQ resonance appearing near 2000 nm wavelength, the results show a significant disparity in energy localization within the odd EDþMQ resonance (highlighted with a double arrow in the figure). We observe that the magnetic energy is mainly localized in the resonances of odd multipoles. This agrees with the observation that odd multipolar resonances are more sensitive to changes in permeability, whereas even multipolar resonances are more sensitive to changes in permittivity (and refractive index). When designing EO metasurfaces, the focus should be on optimizing the excitation and tuning of even multipolar resonances, as these modes demonstrate greater sensitivity to material refractive-index variations. This approach ensures enhanced EO performance and more efficient resonance control.

4.4. Generalization

In addition to nanocuboid antennas, we analyze disk nanoantennas and observe the same trends. Specifically, as the refractive index of the EO material increases, multipolar Mie resonances undergo a redshift, and their spectral prominence is enhanced (Figure S6, Supporting Information). The shift analysis reveals that even multipoles, such as MD and EQ, exhibit the highest sensitivity to refractive index variations, resulting in a more pronounced spectral shift than odd multipoles ED and MQ (Figure S7, Supporting Information). In contrast, odd multipoles, including ED and MQ, demonstrate sensitivity to artificial variations in permeability that is higher than that of even multipoles. This behavior, observed consistently across both the nanocuboid and disk nanoantennas, suggests an universality of the refractive-index-dependent tunability mechanism. The stronger confinement and directional scattering of disk nanoantennas at higher refractive indices further validate the advantage of employing $Sn_2P_2S_6$, or other high-index EO material, over conventional EO materials for highly tunable metasurfaces. These findings are also expected to hold in materials where the refractive index change is driven by mechanisms other than the EO effect, such as thermo-optic effects or phase changes, provided that the nanoantenna material has a refractive index in the same range as considered here and negligible losses.

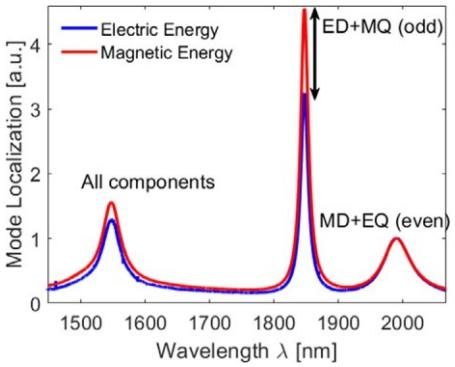

Figure 6. Relative mode localization for electric and magnetic energies. The two spectral profiles are normalized so that the energy in the MDþEQ resonance is the same, and the double arrow indicates the drastic difference in energy localization in the EDþMQ resonance. The results are for a metasurface with $n = 2.7$, array periods $D_x = D_y = 950$ nm, nanocuboids with $a_x = a_y = a_z = 720$ nm, and $w = 80$ nm bridges.

Although EO materials with a higher refractive index allow for stronger nanoantenna resonance (that is, higher mode localization and deeper and broader transmittance dips), in our computations, the resonance shift related to even multipoles is very similar for all EO materials considered, and increasing the refractive index does not provide a substantial advantage. While strong field localization is often reported to enhance EO modulation,[61,62] our analysis shows little impact of this effect. The weak dependence of the EO resonance shift on the metasurface refractive index is unintuitive and contradicts the assumption mentioned earlier that a higher refractive index results in a higher mode localization, stronger optical fields E_w, and therefore, a larger shift under the EO effect. We observe that a higher refractive index results in stronger resonances and deeper features in transmittance spectra associated with higher E_w. Other types of effects, such as nonlinear response and higher-harmonic generation, are commonly determined by the strength of the optical field (with the typical scaling factor $\propto E_w^2$). However, the EO shift does not increase for stronger E_w to the same extent as other processes related to the light-matter interaction.

As we discussed above, Mie resonances are determined by complex expressions involving Mie coefficients and special functions, but some qualitative features can be understood by drawing an analogy with much simpler Fabry–Pérot resonances. In the latter, the resonant state is formed when $m\lambda/n \approx 2L$, where λ is the wavelength of the resonance; n is the refractive index inside the resonator; $m = 1, 2, 3$, etc., is an integer; and L is the characteristic dimension of the resonator. A more accurate expression should account for nonideal reflection from the resonator boundaries (introduced through the complex reflection coefficient), the possibility of multiple nodes in the resonator ($m > 1$), losses, and others, but we use the simplest relation above because it captures the main properties of the resonance shift. A higher refractive index of the resonator n leads to stronger optical confinement and sharper Fabry–Pérot resonances (that is, higher finesse). In this case, with the change in the refractive index of the resonator by Δn, the resonant condition implies $\Delta\lambda \approx 2L\Delta n/m$. Thus, the resonance shift is mainly determined by the change in the refractive index Δn and characteristic dimensions that determine the formation of the resonance, but it has little or no dependence on the strength of the optical field inside the resonator E_w. Thus, our findings indicate that Mie resonances in the EO metasurface exhibit the same behavior as Fabry–Pérot resonances, namely, the primary effect stems from the change Δn, especially for small array periods, with very little dependence on the field in the Mie resonance. We also note that multipolar resonances are very weak in the case of dense arrays

(e.g., weak spectral features in transmittance spectra for $D_x = D_y$ □ 730–750 nm in Figure 3), and this contributes to their little influence on the EO shift in cases of small periods.

We can also consider the case of a continuous film of thickness $L = 720$ nm, the same as the nanoantenna height in the simulations ($a_z = 720$ nm). In this case, resonances in transmission will be determined by the approximate expression $(m - 1/2)\lambda/n \approx 2L$. For $n = 2.7$, the resonance at the wavelength of $\lambda = 7776$ nm ($m = 1$) is shifted by $\Delta\lambda = 144$ nm for $\Delta n = 0.05$, at 2592 nm ($m = 2$) by 48 nm, at 1555 nm ($m = 3$) by 29 nm, and at 1111 nm ($m = 4$) by 21 nm. As we discussed above, the shift $\Delta\lambda$ is the same for the film with refractive indices 2.3 and 3.0, even though the resonances are at different wavelengths (see Table S1, Supporting Information). Thus, for continuous films, larger EO shifts are possible at the longer wavelength, but, overall, they are proportional to Δn, and it is the same functional dependence observed for the metasurfaces. Finally, we compare the transmittance for three different cases of interest: continuous thin film, disk metasurface, and cuboid metasurface (Figure S8, Supporting Information). Apart from the sharp Mie resonances, all the broad spectral features in the cuboid metasurface transmittance closely follow the maxima and minima in the spectra of a continuous thin film with the same refractive index, with only minor deviations in the extrema positions (and depth of the minima). The same broad spectral features are also present in the disk metasurface spectra transmittance, but they are blue-shifted with respect to those in the corresponding thin-film and cuboid cases. For both cuboids and disks, the transmission maxima positions agree well with the estimates based on an effective medium approach (Figure S9, Supporting Information). These observations provide some additional understanding of the overall transmission spectra of nanoantenna metasurfaces (especially broad spectral features) and their dependence on the refractive index of the material.

5. Material Considerations for EO Metasurface Design

We investigated how variations in the refractive index of materials can induce significant shifts in the multipolar Mie resonances to address the challenge of tuning nanoantenna resonances through EO modulation. The application of multipolar decomposition provided the information on the resonant behavior of nanoantennas under varying conditions, leading to a deeper understanding of how to optimize their tunability for various photonic applications. In the calculations above, we obtained results for $\Delta n = 0.05$, and although the resonance shifts are expected to be different, the general conclusion remains valid for larger or smaller Δn. The results described in the previous section indicate that the starting value of the refractive index has a small influence on the magnitude of the EO-induced shifts in resonance position. As such, other physical parameters should be considered when selecting materials to use in dynamic metasurfaces. The primary characteristic to consider should be the magnitude of the EO coefficient, as this determines the overall maximum Δn achievable by applying an external electric field. However, material transparency window, ease of procuring or growing high-quality specimens, and the availability of reliable patterning options should also be taken into consideration.

5.1. Maximum Δn for Room Temperature

As we discussed above, $LiNbO_3$ is the most widely used EO material due to its accessibility in commercial manufacturing. Its largest EO coefficient is $r_{333} = 32$ pm V^{-1} in the visible range, with little wavelength dispersion.[63] We use unclamped coefficients throughout this discussion. The refractive index change induced by the Pockels effect is approximately $|\Delta n| \approx 0.5 n^3 r E$, where E is the applied electric-field bias. The maximum achievable change for $LiNbO_3$ is $\Delta n \approx 0.01$ for $E = 70$ kV mm^{-1}, which is close to the breakdown voltage.[64]

$BaTiO_3$ has much higher EO coefficients but is less common due to the challenges in realizing high-quality specimens. The largest component of the EO tensor is $r_{131} \approx 1000$ pm V^{-1} at a wavelength of 1500 nm and room temperature,[65] but this off-diagonal component cannot be exploited in the type of configuration considered here. The next largest coefficient is $r_{333} \approx 80$ pm V^{-1} at a wavelength of 1500 nm and room temperature.[65] The corresponding maximum refractive index change is $\Delta n \approx 0.15$ assuming a bias of $E = 300$ kV mm^{-1}, which is the breakdown strength reported for very thin films of the material.[66] It should be noted that exploiting r_{333} requires the applied electric field to be parallel to the light polarization. This is not the case for the configuration in Figure 1, but it can be done if the bridges connect the nanoantennas in the x-direction. As discussed earlier, the direction of the bridges does not change the qualitative behavior of the nanoantenna array (see Figure S3, Supporting Information), so r_{333} is used for the remaining discussion of $BaTiO_3$. The relevant parameters for $Sn_2P_2S_6$ are $r_{111} \approx 170$ pm V^{-1} (value reported for 1300 nm, but the dispersion is weak in this spectral range) and $r_{331} \approx 140$ pm V^{-1} at room temperature,[67] leading to $\Delta n = 0.13$ and 0.11, respectively. These estimates assume a breakdown strength comparable to that of $LiNbO_3$, but the actual value has not yet been reported in the literature, to the best of our knowledge. So, at room temperature, both $Sn_2P_2S_6$ and $BaTiO_3$ outperform $LiNbO_3$. It should also be mentioned that because Δn is proportional to n^3, using a higher index material leads to a larger bias-induced change Δn for the same EO coefficient r.

5.2. Curie Temperature

There is another potential advantage of using $Sn_2P_2S_6$ and $BaTiO_3$ instead of $LiNbO_3$: They both have relatively low Curie temperatures (see Table 1). Since the EO effect is enhanced upon approaching the Curie point for at least some of the tensor components, a regime of sizable EO coefficients could be reached by careful control of the device temperature with standard laboratory equipment. For example, for $Sn_2P_2S_6$, $r_{111} \approx 1300$ pm V^{-1} at a temperature of 2 °C below the Curie temperature, which is ≈65 °C.[67] For $BaTiO_3$, no experimental data have been reported for r as a function of temperature. However, an extrapolation based on the temperature dependencies of other physical parameters yields r_{333}(633 nm) ≈350 pm V^{-1} at 100 °C,[65] which is still more than 30 °C below the Curie temperature. Then, using the same wavelength dispersion as at room temperature, we

estimate r_{333}(1500 nm) □250 pm V^{-1} at 100 °C. Although this is strictly not correct, it is a sufficient approximation for our purposes.

5.3. Realistic Bias

The operation of an EO device close to the electric breakdown is problematic. For the remainder of this section, we assume operation at 20 kV mm^{-1}. Even though this is probably still unrealistic, as it would imply the use of 1000 V across a 50-μm-wide structure, it is significantly below the expected breakdown strength and provides a point of comparison among materials. The field strength of 20 kV mm^{-1} is considered only for estimating the upper limit of refractive index modulation, while practical operation would involve voltages of several to tens of volts.

Under these electric field conditions, at room temperature, the maximum refractive index change for $BaTiO_3$ is Δn = 0.01 and for $Sn_2P_2S_6$ is Δn = 0.03. Figure 7 shows the resonance shifts for nanoantenna arrays with 950 nm periods as a function of Δn. The vertical dotted lines represent the behavior at 20 kV mm^{-1} and room temperature. It can be seen that, with both materials, only a few-nanometer shift can be obtained at room temperature. In contrast, using the higher temperature value of r_{333} mentioned above and the same voltage, Δn □ 0.03 for $BaTiO_3$ (see dashed magenta line in the figure), corresponding to resonance shifts of about 20 nm for the MDþEQ mode. Significantly larger shifts should be possible at even higher temperatures. However, a better estimate of the upper limit is not possible without additional experimental data on this material. For $Sn_2P_2S_6$, Δn □ 0.25, indicating that the full range of resonance shifts in Figure 7a is, in principle, attainable. Figure S10, Supporting Information, shows the case of the periods 730 nm for $Sn_2P_2S_6$, and the observed trends are similar to those discussed here for the period of 950 nm.

Thus, much larger changes in refractive index and, consequently, resonance shift could be achieved in $Sn_2P_2S_6$ and $BaTiO_3$ metasurfaces than in the metasurfaces with $LiNbO_3$ or other EO materials with a similarly high Curie temperature (>500 °C), such as $LiTaO_3$. It should be mentioned that the operation of a device near the Curie temperature of an EO material is not trivial. For example, any temperature fluctuation will result in a shift in the device's resonance, which is going to be detrimental to many device concepts. The closer the system is to the Curie temperature, the larger the instability issues will be. The refractive indices of the unbiased material also depend on the temperature, but these changes are relatively small and do not exhibit a peak near the Curie temperature.[68,69] The main effect of these changes is to slightly shift the position of the resonance in the absence of the field; the impact on the electric-field-induced shifts would be small and would not change the general trends. Additionally, the permittivity increases when approaching the Curie temperature, which will affect the magnitude of the potential difference needed to achieve a given electric field inside a material, and dielectric losses arise, which could limit the operating speed of the device. However, the possible advantages of devices with very large tuning ranges should warrant exploration of this approach experimentally, as well as accompanying simulation work in which these higher-order temperature effects are considered.

Also of interest is the identification of EO materials with a higher refractive index. Currently, there are only very few known EO materials with a refractive index of 3.0 or higher. One of these is GaAs and CdTe, but their EO coefficients are very small.[70] We also note that the GaAs and CdTe crystal structures are centrosymmetric, and they lack spontaneous polarization. Thus, GaAs and CdTe are not ferroelectric and do not exhibit a Curie temperature associated with a ferroelectric to paraelectric transition.[71] Consequently, materials of this type would not exhibit a significant enhancement of the EO effect with temperature. Potential material classes to consider for obtaining a higher refractive index are other III–V compounds, II–VI compounds, or chalcogenides containing Se or Te, because their higher density compared to those containing S should result in a larger refractive index.

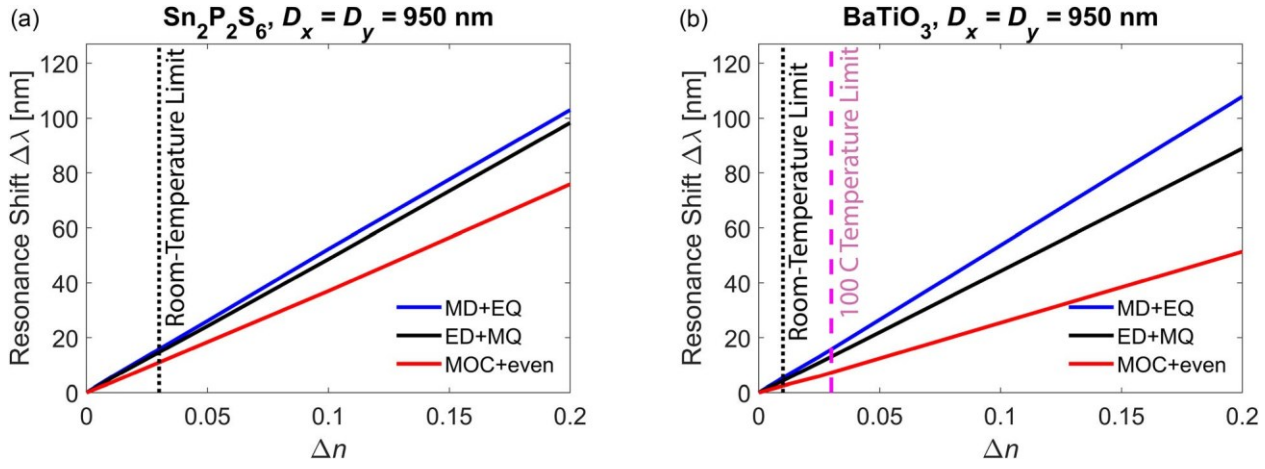

Figure 7. Shift of resonance wavelength as a function of EO-induced refractive index change for a) $Sn_2P_2S_6$ and b) $BaTiO_3$. The black dotted lines in both panels correspond to the shift achievable at room temperature and 20 kV mm^{-1} (Δn = 0.03 in (a) and Δn = 0.01 in (b)). The magenta dashed line in the $BaTiO_3$ case indicates the shift obtainable at 100 °C for the same electric field (Δn = 0.03). For $Sn_2P_2S_6$, the full Δn range is accessible at 20 kV mm^{-1} by increasing the temperature toward the Curie point. The results are for a metasurface with array periods D_x = D_y = 950 nm, nanocuboids with a_x = a_y = a_z = 720 nm, and w = 80 nm bridges.

To sum up, the strong EO response of $Sn_2P_2S_6$ and $BaTiO_3$ and their low Curie temperature T_c in combination with tailored metasurface designs can be used to achieve tunable modulation throughout the targeted optical range. However, given the higher refractive index of $Sn_2P_2S_6$ compared to $BaTiO_3$, a metasurface made of $Sn_2P_2S_6$ should provide somewhat better performance in cases where a higher mode localization and stronger multipolar resonances are preferable. However, as mentioned in the previous section, EO-induced resonance shifts are comparable over a wide range of refractive-index values.

6. Conclusions

We considered nanoantennas made of various known EO materials. Our results provide a strong foundation for further exploration and optimization of EO metasurfaces as suitable devices with actively controllable characteristics. The ability to modulate the refractive index with an applied electric-field bias allows for effective control of these resonances, leading to more efficient and adaptive photonic devices. By analyzing nanoantenna arrays made of EO materials with various refractive indices, we identify a pattern in how the refractive index affects the nature of multipolar Mie resonances and, specifically, their tunability.

We employed electromagnetic duality, allowing a comprehensive analysis of the interplay between electric and magnetic responses. We showed that even multipoles, such as MD and EQ, are highly sensitive to refractive index variations in the metasurface, while odd multipoles, including ED and MQ, respond most strongly to changes in permeability. Achievable resonance shifts for a given change in refractive index decrease slightly when the array period increases, but exhibit only a weak dependence on the refractive index itself.

Still, a higher refractive index enhances light confinement and interaction in the metastructure, and thus, the utilization of higher refractive index materials is desirable. Additionally, large EO coefficients are required to achieve wide tuning ranges. Chalcophosphate $Sn_2P_2S_6$ is a promising candidate, as it possesses one of the highest refractive indices among known EO materials, a high EO coefficient, and a low Curie temperature, allowing substantial EO tuning near this threshold under moderate electric-field bias. The practical realization of the $Sn_2P_2S_6$ metastructures is contingent on the availability of single-crystal specimens of sufficient quality and appropriate form factor. Suitable patterning processes and conditions will need to be investigated before functional metasurfaces can be realized. Patterning approaches for $BaTiO_3$ are also of interest, as this platform can serve as a proof-of-principle demonstration of resonance tuning as a function of electric field and temperature.

Among the resonances, those related to even multipoles exhibit a higher sensitivity to variations in the metasurface refractive index than odd multipoles. Thus, the design of metasurfaces should focus on optimizing such resonances to facilitate their excitation and tuning. The findings of this work are significant for the development of next-generation tunable optical technologies. By exploring the integration of EO crystals with other materials in hybrid structures, we aim to uncover their potential for the development of multifunctional photonic devices. Using the dynamic control enabled by the EO materials, applications such as beam steering, reconfigurable optical filters, and adaptive lenses could be significantly improved. This research paves the way for more versatile and power-efficient photonic systems, which expand their use in fields ranging from telecommunications to imaging and sensing, where real-time adjustment of optical properties is crucial.

Supporting Information

Supporting Information is available from the Wiley Online Library or from the author.

Acknowledgements

This research was supported in part by the Air Force Research Laboratory's Materials and Manufacturing Directorate, through the Air Force Office of Scientific Research Summer Faculty Fellowship Program, Contract Numbers FA8750-15-3-6003, FA9550-15-0001, and FA9550-20-F-0005. V.E.B. work is partly supported by the U.S. National Science Foundation under grant no. 2418519.

Conflict of Interest

The authors declare no conflict of interest.

Data Availability Statement

The data that support the findings of this study are available from the corresponding author upon reasonable request.

Keywords

barium titanate, chalcophosphate, lithium niobate, perovskites, $Sn_2P_2S_6$

Received: May 20, 2025
Revised: November 8, 2025
Published online:

[1] M. Brongersma, *Nat. Photonics* 2008, *2*, 270.
[2] A. B. Evlyukhin, S. M. Novikov, U. Zywietz, R. L. Eriksen, C. Reinhardt, S. I. Bozhevolnyi, B. N. Chichkov, *Nano Lett.* 2012, *12*, 3749.
[3] A. B. Evlyukhin, C. Reinhardt, U. Zywietz, B. N. Chichkov, *Phys. Rev. B* 2012, *85*, 245411.
[4] V. G. Kravets, A. V. Kabashin, W. L. Barnes, A. N. Grigorenko, *Chem. Rev.* 2018, *118*, 5912.
[5] A. Han, J. V. Moloney, V. E. Babicheva, *J. Chem. Phys.* 2022, *156*, 114104.
[6] V. E. Babicheva, *Nanomaterials* 2024, *14*, 1539.
[7] Y. Jiang, J. Zhang, J. Ma, D. N. Neshev, A. A. Sukhorukov, *APL Quantum* 2025, *2*, 026115.
[8] V. E. Babicheva, C.-C. Chang, *ACS Omega* 2025, *10*, 23150.
[9] H. Yang, W. Mills, S. Bharadwaj, S. Desai, T. Santiago-Cruz, S. Prescott, O. Mitrofanov, I. Brener, J. Schuller, Z. Jacob, P. P. Iyer, *Adv. Opt. Mater.* 2025, *13*, 2402755.
[10] A. Romero, V. E. Babicheva, *J. Appl. Phys.* 2024, *136*, 083106.
[11] J. Yang, S. Gurung, S. Bej, P. Ni, H. W. Howard Lee, *Rep. Prog. Phys.* 2022, *85*, 036101.
[12] A. I. Kuznetsov, M. L. Brongersma, J. Yao, M. K. Chen, U. Levy, D. P. Tsai, N. I. Zheludev, A. Faraon, A. Arbabi, N. Yu, D. Chanda, K. B. Crozier, A. V. Kildishev, H. Wang, J. K. W. Yang,

J. G. Valentine, P. Genevet, J. A. Fan, O. D. Miller, A. Majumdar, J. E. Fröch, D. Brady, F. Heide, A. Veeraraghavan, N. Engheta, A. Alù, A. Polman, H. A. Atwater, P. Thureja, R. Paniagua-Dominguez, et al., *ACS Photonics* 2024, *11*, 816.
[13] P. Berini, *ACS Photonics* 2022, *9*, 2204.
[14] R. Kanyang, C. Fang, Q. Yang, Y. Shao, G. Han, Y. Liu, Y. Hao, *Nanomaterials* 2022, *12*, 3179.
[15] D. Kang, H. Heo, Y. Yang, J. Seong, H. Kim, J. Kim, J. Rho, *Opto. Electron. Adv.* 2024, *7*, 230216.
[16] H. Weigand, V. V. Vogler-Neulg, M. R. Escala, D. Pohl, F. U. Richter, A. Karvounis, F. Timpu, R. Grange, *ACS Photonics* 2021, *8*, 3004.
[17] A. Weiss, C. Frydendahl, J. Bar-David, R. Zektzer, E. Edrei, J. Engelberg, N. Mazurski, B. Desiatov, U. Levy, *ACS Photonics* 2022, *9*, 605.
[18] A. Forouzmand, M. M. Salary, G. K. Shirmanesh, R. Sokhoyan, H. A. Atwater, H. Mosallaei, *Nanophotonics* 2019, *8*, 415.
[19] J. Tian, H. Luo, Y. Yang, F. Dg, Y. Qu, D. Zhao, M. Qiu, S. I. Bozhevolnyi, *Nat. Commun.* 2019, *10*, 396.
[20] F. Dg, Y. Yang, S. I. Bozhevolnyi, *Adv. Opt. Mater.* 2019, *7*, 1801709.
[21] T. Lewi, H. A. Evans, N. A. Butakov, J. A. Schuller, *Nano Lett.* 2017, *17*, 3940.
[22] Y. Yan, H. Zhang, X. Liu, L. Peng, Q. Zhang, G. Yu, Q. Wu, H. Li, *Laser Photonics Rev.* 2025, *19*, 2400624.
[23] C.Damgaard-Carstensen,S.I.Bozhevolnyi,*Nanophotonics* 2023,*12*,2953.
[24] H. C. Weigand, U.-L. Talts, A.-L. Vieli, V. V. Vogler-Neulg, A. Nardi, R. Grange, *Nano Lett.* 2024, *24*, 5536.
[25] J. Sun, Z. Chai, Y. Yang, Z. Cui, Y. Xu, Y. Xu, Y. Fu, H. Yuan, *Nanoscale* 2025, *17*, 2700.
[26] S. L, Y. Chen, T. Hwang, A. Upadhyay, R. Rady, D. Dolt, S. Palermo, K. Entesari, C. Madsen, Z. J. Wong, S. Lan (Preprint), arXiv 2501.06102, v1, Submitted: Jan. 2025.
[27] V. E. Babicheva, M. Rumi, *RSC Adv.* 2024, *14*, 33906.
[28] V. E. Babicheva, M. Rumi, *in Plasmonics: Design, Materials, Fabrication, Characterization, and Applications XXII*, Vol. *13111* (Eds: T. Tanaka, Y.-J. Lu), Ternational Society for Optics and Photonics. SPIE, San Diego, CA 2024, p. 1311102.
[29] Y. Li, Z. Huang, W. Qiu, J. Dong, H. Guan, H. Lu, *Chese Opt. Lett.* 2021, *19*, 060012.
[30] C. Fang, R. Kanyang, Y. Ji, Y. Zhang, J. Yang, D. Wang, Y. Liu, X. Gan, G. Han, Y. Hao, *Laser Photonics Rev.* 2024, *18*, 2300900.
[31] L. Carletti, A. Zilli, F. Moia, A. Toma, M. Fazzi, C. De Angelis, D. N. Neshev, M. Celebrano, *ACS Photonics* 2021, *8*, 731.
[32] R. Liu, C. Zhou, *Opt. Lett.* 2023, *48*, 6565.
[33] X. Lv, S. Wu, Z. Tian, Y. Li, T. Yang, W. Qiu, H. Guan, H. Lu, *J. Opt. Soc. Am. B* 2023, *40*, D15.
[34] S. Liu, W. Hong, X. Sui, X. Hu, *Photonics* 2023, *10*, 661.
[35] Y. Zhao, Z. Chen, C. Wang, Y. Yang, H. Sun, *Nanoscale* 2023, *15*, 12926.
[36] G. Chen, N. Li, J. D. Ng, H.-L. L, Y. Zhou, Y. H. Fu, L. Y. T. Lee, Y. Yu, A.-Q. Liu, A. J. Danner, *Adv. Photonics* 2022, *4*, 034003.
[37] Y. Xie, M. Nie, S.-W. Huang, *Appl. Phys. Lett.* 2024, *124*, 051108.
[38] A. Fedotova, L. Carletti, A. Zilli, F. Setzpfandt, I. Staude, A. Toma, M. Fazzi, C. De Angelis, T. Pertsch, D. N. Neshev, M. Celebrano, *ACS Photonics* 2022, *9*, 3745.
[39] B. Gao, M. Ren, W. Wu, W. Cai, J. Xu, *Sci. Cha Phys., Mech. Astronomy* 2021, *64*, 240362.
[40] L. Wang, I. Shadrivov, *Opt. Express* 2022, *30*, 35361.
[41] L. Wang, F. Setzpfandt, I. Shadrivov, *Opt. Mater. Express* 2023, *13*, 3376.
[42] S. Ramakrishnan, N. Khatri, R. Tirumala, F. Mohammadparast, K. Karuppasamy, A. Kalkan, M. Andiappan, *J. Phys. Chem. C* 2022, *126*, 16272.
[43] A. García-Etxarri, R. Gómez-Meda, L. S. Froufe-Pérez, C. López, L. Chantada, F. Scheffold, J. Aizpurua, M. Nieto-Vesperas, J. J. Sáenz, *Opt. Express* 2011, *19*, 4815.
[44] S. Zhang, R. Jiang, Y.-M. Xie, Q. Ruan, B. Yang, J. Wang, H.-Q. Lin, *Adv. Mater.* 2015, *27*, 7432.
[45] J. Fan, Z. Li, Z. Xue, H. Xg, D. Lu, G. Xu, J. Gu, J. Han, L. Cong, *Opto-Electron. Sci.* 2023, *2*, 230006.
[46] Y. Hou, Y. Xu, B. Du, Y. Zhang, L. Zhang, *Opt. Lett.* 2024, *49*, 470.
[47] J. Zhang, B. Pan, W. Liu, D. Dai, Y. Shi, *Opt. Express* 2022, *30*, 20839.
[48] G. Liu, S. Zong, X. Liu, J. Chen, Z. Liu, *Opt. Lett.* 2024, *49*, 113.
[49] Z. Han, F. Dg, Y. Cai, U. Levy, *Nanophotonics* 2021, *10*, 1189.
[50] Z. Ye, Y. Fan, K. Sun, W. Qiu, H. Wang, H. Shi, Y. Zeng, F. Zhang, *Opt. Quantum Electron.* 2024, *56*, 2002.
[51] A. B. Evlyukh, V. R. Tuz, *Phys. Rev. B* 2023, *107*, 155425.
[52] I. Loulas, E. Almpanis, M. Kouroublakis, K. L. Tsakmakidis, C. Rockstuhl, G. P. Zouros, *ACS Photonics* 2025, *12*, 1524.
[53] R. Alaee, C. Rockstuhl, I. Fernandez-Corbaton, *Adv. Opt. Mater.* 2019, *7*, 1800783.
[54] M. Poleva, K. Frizyuk, K. Baryshnikova, A. Evlyukh, M. Petrov, A. Bogdanov, *Phys. Rev. B* 2023, *107*, L041304.
[55] T. Wu, A. B. Evlyukh, V. R. Tuz, *Phys. Rev. B* 2024, *110*, 115408.
[56] I. Allayarov, A. B. Evlyukh, A. C. Lesa, *Opt. Express* 2024, *32*, 5641.
[57] V. E. Babicheva, J. V. Moloney, *Laser Photonics Rev.* 2019, *13*, 1800267.
[58] V. Karimi, V. E. Babicheva, *Opt. Express* 2023, *31*, 16857.
[59] V. E. Babicheva, A. B. Evlyukh, *Phys. Rev. B* 2019, *99*, 195444.
[60] W. Wang, M. Ramezani, A. I. Va¨keva¨en, P. Törma¨, J. G. Rivas, T. W. Odom, *Mater. Today* 2018, *21*, 303.
[61] Y. Tang, H. Chen, Y. Li, X.-q. Luo, L. Jin, X.-l. Wang, *Opt. Express* 2024, *32*, 40007.
[62] M. Li, J. Lg, Y. He, U. A. Javid, S. Xue, *Nat. Commun.* 2020, *11*, 4123.
[63] R. S. Weis, T. K. Gaylord, *Appl. Phys. A* 1985, *37*, 191.
[64] M. Luennemann, U. Hartwig, G. Panotopoulos, K. Buse, *Appl. Phys. B* 2003, *76*, 403.
[65] P. Bernasconi, M. Zgonik, P. Gunter, *J. Appl. Phys.* 1995, *78*, 2651.
[66] H. Wu, P. Ponath, E. L. Lin, R. M. Wallace, C. Young, J. G. Ekerdt, A. A. Demkov, M. R. McCartney, D. J. Smith, *J. Vac. Sci. Technol. B* 2020, *38*, 044007.
[67] D. Haertle, G. Caimi, A. Haldi, G. Montemezzani, P. Günter, A. A. Grabar, I. M. Stoika, Y. M. Vysochanskii, *Opt. Commun.* 2003, *215*, 333.
[68] S. Wemple, M. Didomenico, I. Camlibel, *J. Phys. Chem. Solids* 1968, *29*, 1797.
[69] D. Haertle, A. Guaro, J. Hajfler, G. Montemezzani, P. Günter, *Opt. Express* 2005, *13*, 2047.
[70] G. L. Herrit, H. E. Reedy, *MRS Onle Proc. Library* 1989, *152*, 169.
[71] R. Weil, R. Nkum, E. Muranevich, L. Benguigui, *Phys. Rev. Lett.* 1989, *62*, 2744.
[72] E. C. Subbarao, *Ferroelectrics* 1973, *5*, 267.
[73] B. Zysset, I. Biaggio, P. Günter, *J. Opt. Soc. Am. B* 1992, *9*, 380.
[74] M. Zgonik, R. Schlesser, I. Biaggio, P. Günter, *Ferroelectrics* 1994, *158*, 217.
[75] S. H. Wemple, J. M. DiDomenico, I. Camlibel, *Appl. Phys. Lett.* 1968, *12*, 209.
[76] W. L. Bond, *J. Appl. Phys.* 1965, *36*, 1674.
[77] K. Onuki, N. Uchida, T. Saku, *J. Opt. Soc. Am.* 1972, *62*, 1030.
[78] D. E. Zelmon, D. L. Small, D. Jundt, *J. Opt. Soc. Am. B* 1997, *14*, 3319.
[79] I. Camlibel, M. Didomenico, S. Wemple, *J. Phys. Chem. Solids* 1970, *31*, 1417.
[80] D. E. Zelmon, D. L. Small, P. Schunemann, *MRS Onle Proc. Library* 1997, *484*, 537.
[81] J. Moreau, C. Michel, R. Gerson, W. James, *J. Phys. Chem. Solids* 1971, *32*, 1315.
[82] S. Chu, D. Sgh, J. Wang, E.-P. Li, K. Ong, *Laser & Photonics Rev.* 2012, *6*, 684.
[83] D. Sando, P. Hermet, J. Allibe, J. Bourderionnet, S. Fusil, C. Carrétéro, E. Jacquet, J.-C. Mage, D. Dolfi, A. Barthélémy, P. Ghosez, M. Bibes, *Phys. Rev. B* 2014, *89*, 195106.